Bioorganic Chemistry 91 (2019) 103165

Contents lists available at ScienceDirect

Bioorganic Chemistry

journal homepage: www.elsevier.com/locate/bioorg

A combined experimental and computational study on peptide nucleic acid (PNA) analogues of tumor suppressive miRNA-34a

Valerio Piacenti[a,1], Emma Langella[b,1], Ida Autiero[b], John C. Nolan[c], Olga Piskareva[c], Mauro F.A. Adamo[a], Michele Saviano[d], Maria Moccia[d,*]

[a] RCSI, Dept. of Pharmaceutical & Medicinal Chemistry, 123 St Stephen's Green, Dublin 2, Ireland
[b] National Research Council (CNR)-IBB, via Mezzocannone 16, 80134 Naples, Italy
[c] RCSI, Dept. of Cancer Genetics, York Street, Dublin 2, Ireland
[d] National Research Council (CNR)-IC, via G. Amendola 122/O, 70126 Bari, Italy

ARTICLE INFO

Keywords:
PNA
MiRNA-34a
Tumor suppressive
Molecular dynamics

ABSTRACT

MicroRNAs are a ubiquitous class of non-coding RNAs able to regulate gene expression in diverse biological processes. Widespread miRNAs deregulation was reported in numerous diseases including cancer, with several miRNAs playing oncogenic and/or tumor suppressive role by targeting multiple mRNAs simultaneously. Based on these findings, miRNAs have emerged as promising therapeutic tools for cancer treatment. Herein, for the first time, peptide nucleic acids (PNAs) were studied to develop a new class of molecules able to target 3′UTR on MYCN mRNA without a fully complementary base pairing sequence (as miRNAs). For our proof of concept study we have selected as a model the miRNA-34a, which acts as a tumor suppressor in a number of cancers including neuroblastoma. In particular, miRNA-34a is a direct regulator of MYCN oncogene, whose overexpression is a prominent biomarker for the highly aggressive neuroblastoma phenotype. The design and synthesis of three PNA-based oligomers of different length was described, and their interaction with two binding sites on the target MYCN mRNA was investigated by molecular dynamics simulation, and spectroscopic techniques (CD, UV). Intake assay and confocal microscopy of PNA sequences were also carried out *in vitro* on neuroblastoma Kelly cells. Despite the presence of multiple mismatches, the PNA/RNA hetero duplexes retain very interesting features in terms of stability, affinity as well as of cellular uptake.

1. Introduction

MicroRNAs (miRNAs) represent a class of short (19–25 nts) non coding RNAs, which have emerged as major cellular regulators [1], playing a crucial role in a wide range of biological processes including cell differentiation, proliferation and apoptosis [2]. They are processed from longer primary transcripts, followed by maturation steps involving endonuclease enzymes Drosha (in the nucleus) and Dicer (in the cytoplasm) [1,3]. MiRNAs are able to bind mRNAs at the 3′ untranslated regions (UTRs) via partial complementarity, whereas target recognition is primarily driven by "seed" region (positions 2–8 nts at the miRNA's 5′ end, which designate miRNA families) full complementarity, leading to down-regulation of mRNA and protein levels [3,4]. Furthermore, aberrant miRNA expression is present in several diseases such as hepatitis [5], cardiovascular disease [6] and cancer [7], and it is now proven that miRNAs play a significant role in cancer occurrence, progression and metastasis [8]. As a result, miRNAs can be attractive tools and targets for novel therapeutic approaches [9]. In particular, the therapeutic potential offered by miRNAs, is based on the ability of one miRNA to target multiple genes that are dysregulated in cancer [2,10], thus orchestrating multiple pathways at the same time, either as tumor suppressors miRs or as tumor promoters (oncomirs) [11]. Two main therapeutic strategies are based on miRNAs: miRNA inhibition therapy, which involves inhibition of overexpressed oncomiRNAs and miRNA replacement therapy, which involves replacing tumor suppressive miRNA's expression normally repressed [10]. The oncomiRs targeting can be achieved by using antisense oligonucleotide AMO (anti-miRNA antisense oligomer), or antagomirs made of two′-O-methyl (2′-OMe), two′-O-methoxyethyl (2′-MOE), 2′-fluoro/2′-methoxyethyl (2′-F/MOE) with a phosphorothioate modified backbone, which are more stable compared to unmodified RNA [12]. Locked nucleic acids (LNAs) and PNAs have also been successfully employed to increase the efficiency of

---

* Corresponding author.
E-mail address: maria.moccia@cnr.it (M. Moccia).
[1] These authors contributed equally to this work.

https://doi.org/10.1016/j.bioorg.2019.103165
Received 11 December 2018; Received in revised form 19 July 2019; Accepted 29 July 2019

synthetic oligonucleotides to target miRNAs [12]. Two additional strategies can be used to block miRNA function: miRNA sponge and miRNA mask based approach [13]. A miRNA "sponge" contains multiple target sites and has the ability to bind various miRNAs simultaneously preventing them to target the mRNA. A miRNA mask [13] oligonucleotide is a single-stranded oligonucleotide perfectly complementary to the miRNA binding sites (3′ UTR mRNAs) which impedes endogenous oncogenic miRNA to exert their undesired function. In the case of miRNA replacement therapy, tumor suppressor miRNAs are replaced to restore lost function resulting from downregulation of key-miRNAs (such as miRNA-34a and let-7a) [14]. The most common design for a synthetic miRNA mimic is a double-stranded RNA, made of a guide strand (the one actively recognizing the target) having an identical nucleotide sequence to the miRNA to be replaced, and a passenger strand (originally paired to the guide strand, which is discarded during the mechanism of action) perfectly complementary to the guide. The use of double-stranded miRNA mimics has some drawbacks for drug development [15], therefore chemically modified single-stranded miRNA mimics of miR-124, miR-122 miR-34a and miR-216b were recently developed showing promising effect [16]. The choice of pattern sequence modifications and the type of chemical modification is crucial [16]. Up to now, the number of different modifications employed is relatively small, and the investigation of this chemical space would provide a wide scope for the development of novel therapeutic agents with enhanced activity [15]. In this setting, Peptide Nucleic Acids (PNAs) are a promising class of DNA/RNA analogues [17], able to bind complementary DNA and RNA sequences with high affinity and specificity by forming complexes of extraordinary stability [18]. As a consequence, the thermal stability of PNA–DNA and PNA-RNA duplexes is higher compared to DNA-DNA or DNA-RNA ones [19,20]. PNAs having a pseudo-peptide backbone made of N-(2 aminoethyl) glycine (*aeg*) replacing the natural sugar phosphate, are resistant to enzymatic degradation [21]. PNAs are stable across a wide range of temperatures and pHs and can be easily conjugated to peptide carriers to enhance their solubility and the cell permeability [22,23]. To date, PNAs have been successfully employed in diagnostic, pharmaceutical, therapeutic fields [24]; more recently as anti-miRNA based therapeutics [25] and target protectors [26]. To further expand PNAs emerging role in therapeutics field we have investigated their novel potential use starting from miRNA-34a platform [27]. In particular, for the first time, PNAs were studied to develop a new class of molecules able to target 3′UTR through non-perfect base pairing (as miRNAs do), hence, not belonging to antisense class of molecules (which have full complementarity to a specific sequence on the mRNA) nor miRNA-mask (which requires full complementarity to the 3′UTR mRNA). The miRNA-34a–MYCN axis is a well characterized relationship [28], since MYCN oncogene is a direct target of tumor suppressor miRNA-34a in many cancers [29], including Neuroblastoma (NBL). For this reason miRNA-34a–MYCN has been selected as a model system to test our proof of concept study for PNA-based miRNA analogues. NBL is the most common paediatric solid tumor [30,31], with a heterogeneous clinical behaviour; MYCN amplification, with subsequent MYCN protein overexpression, represents the most significant molecular biomarker, which occurs in 25–30% of NBL tumours [32–34]. The discovery of a close reciprocal relationship between the MYCN oncogene and multiple miRNAs, with MYCN simultaneously the target of miRNA-mediated mechanisms [29] and a miRNA regulator in NBL [35], focused our interest on this system. Furthermore, it has been demonstrated that miRNA-34a is the most potent regulator of MYCN protein expression by binding to the 3′UTR of MYCN mRNA hence, silencing its translation into MYCN protein (Fig. 1) [29,36]. PNAs have been previously used to target MYCN by antisense or antigene approach. Indeed, an antisense PNA was reported by Pession et al. [37]; to target a unique sequence at 5′UTR of N-myc for the selective inhibition of N-myc in two types of NBL cells (N-myc-amplified and unamplified). In the N-myc amplified cells the antisense PNA caused N-MYC translation inhibition, accumulation of cells in G1, induction of differentiation and apoptosis. Shortly after an antigene PNA oligomer was designed by Tonelli et al. [38] to target a sequence in the DNA strand of exon 2 of MYCN to selectively inhibit MYCN transcription. A significant inhibition of MYCN expression by the antigene PNA was achieved in both MYCN-amplified and unamplified cell lines. These findings encouraged the development of PNA-based tumor-specific molecule for neuroblastoma (or other disease) with N-myc overexpression. Indeed, the targeting of MYCN through its relationship with miRNA-34a by PNA-based analogues would be an innovative approach, which takes advantages of PNAs higher affinity for target nucleic acids, their physiological stability, versatility and the unique opportunity to use bioconjugates to promote intracellular delivery.

Herein, we describe the design and synthesis of PNA-based analogues of miRNA-34a of different length, and investigate their interaction with the target MYCN mRNA (Fig. 1) using molecular dynamics simulations as well as spectroscopic studies (UV, CD). Finally, preliminary *in vitro* tests on Kelly NBL cells including intake assay and confocal microscopy were carried out.

2. Results and discussion

2.1. Design and synthesis of PNA as miRNA-34a analogue

PNA-based miRNA-34a sequences of different length were designed, synthetized and evaluated for their ability to bind to MYCN mRNA (a validated miRNA-34a target) [29]. In particular, miRNA-34a binds to the mRNA 3′UTR at two different positions named binding site 1 and 2 (Fig. 1) leading to the translational repression of the MYCN protein [29]. Canonical miRNA binding involves base pairing of the miRNA "seed" region (nucleotides 2–8) to complementary target sites (as shown in Fig. 1). The key role of the seed region in target recognition has been widely described [39] but the stabilization of the duplex induced by "non-seed" nucleobases still needs to be further investigated. In particular, it is reported that the 3′ supplementary region (nucleotides 13–16) also has a considerable role in stabilizing miRNA-target interaction but the extent to which this influences the hybridization depends on each case [40].

Therefore, miRNA-34a guide strand was used as model template to design PNA-based oligomers of different length (Fig. 2), obtained by cutting endogenous miRNA-34a sequence at different key-points to generate: (1) a 22 unit PNA sequence possessing identical sequence to endogenous miRNA-34a; (2) a 17-unit PNA including the regions corresponding to miRNA seed (2–8 nucleobases) and the 3′-supplementary region (13–16 nucleobases), hereafter named seed* and 3′ supplementary* respectively; (3) a 8-unit PNA which includes only the seed* region (Fig. 2). Based on sequences 1–3 (Fig. 2), two sets of PNA oligomers were synthesized: (1) PNA 1–3 (entry 1–3 Table 1) for structural studies; (2) PNA1-3 FITC oligomers (Fig. 3 and Table 1 entries 4–6) for preliminary cell studies. All the PNA sequences included a short peptide carrier constituted by three positively charged lysine residues at the C-terminus (trilysines-peptide-K3 in Fig. 3) to increase water solubility.

In addition, PNA 1–3 FITC sequences also included (a) a lysine and cysteine residue at the N-terminus (CK in Fig. 3) to enhance PNAs cellular uptake and increase water solubility [41]; (b) a 6-aminohexanoic acid as the spacer (spacer, Fig. 3) and (c) a fluorescent tag FITC (fluorescein isothiocyanate, FITC in Fig. 3) to monitor PNAs cellular localization. All the PNA sequences (entries 1–6 Table 1) were prepared by microwave-assisted solid phase peptide synthesis (SPPS) using commercially available Fmoc/Bhoc monomers; exploiting a synthetic protocol previously reported by Fabani [41], which in our laboratory was adapted to a non-automated microwave synthesizer (CEM Discover) on a smaller scale.

The use of microwave assisted synthesis was particularly useful to reduce chain aggregation, considering the length of the sequences, the high CG content, and to improve coupling efficiency [42]. The PNA oligomers were all synthesized in good yield, higher compared to that

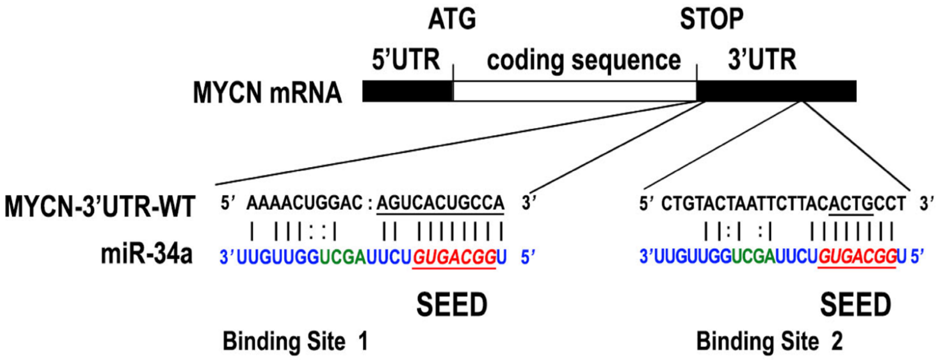

Fig. 1. Schematic representation of miRNA-34a binding site on 3′UTR MYCN mRNA; seed region is reported in red and the 3′supplementary in green.

obtained with standard solid phase peptide synthesis especially for longer sequences (5% compared to 9%). The results obtained were quite in agreement with the literature considering that MBHA rink amide resin was employed instead of Chem-Matrix used by Fabani [41], which according to his work has a positive impact on the yield. In addition, PNA3-FITC included 29 units in total with 50% content of cytosine and guanine nucleobases, which is commonly considered as a threshold for the synthetic feasibility of a PNA sequence. After the synthesis, the oligomers were detached from the solid support, deprotected, precipitated in cold diethyl ether and lyophilized. The purification of the products was carried out using RP-HPLC and the identity of the products was confirmed by MS analysis.

2.2. Computational studies: molecular dynamics simulations

All-atoms Molecular Dynamics (MD) simulations were employed to study the interaction between PNA1-3 of different length (entry 1–3 in Table 1) and the target 3′UTR MYCN mRNA by using GROMACS package [43] and the force field parameters derived for PNAs in our previous works [44]. In detail, two sets of PNA-RNA hybrids, relative to the two MYCN binding sites (Fig. 1), were simulated to gain insights into their structural and dynamic features. A schematic representation of the two sets (containing six RNA/PNA complexes) is shown in Fig. 4: the two MYCN mRNA fragments were named, respectively, RNA1 (blue) and RNA2 (green) and pairwise aligned against matching PNA1-3 (red) having different length.

For all the simulated systems we computed the RMSD (Root Mean Square Deviation) to evaluate the structural changes over the course of the simulation. RMSD was computed for the whole PNA and RNA strands (Fig. 5, A and B), as well as the fully complementary seed* region (Fig. 5, C and D). Inspection of Fig. 5 (A and B) reveals that RNA strands reach higher RMSD values compared to the corresponding PNA strands, suggesting a major flexibility of RNA strands compared to the PNA ones. In particular, RNA strands undergo significant rearrangements (high RMSD values of 1.5 nm) in the two systems containing the short PNA3 strand (RNA1/PNA3 and RNA2/PNA3), due to the absence of the PNA counterpart for non-seed* RNA residues, which are free to move. The RMSD analysis in the seed* regions (of both PNA and RNA strands) is useful to evaluate the influence on the seed stability when modulating the length of the partially-complementary PNA hybrid strand. For all the duplexes, seed* regions rapidly reach equilibrium and show low RMSD values, ranging from 0.15 nm to 0.3 nm, thus suggesting that the fully complementary seed* regions are stable and their conformations are rather unchanged compared to the starting ones

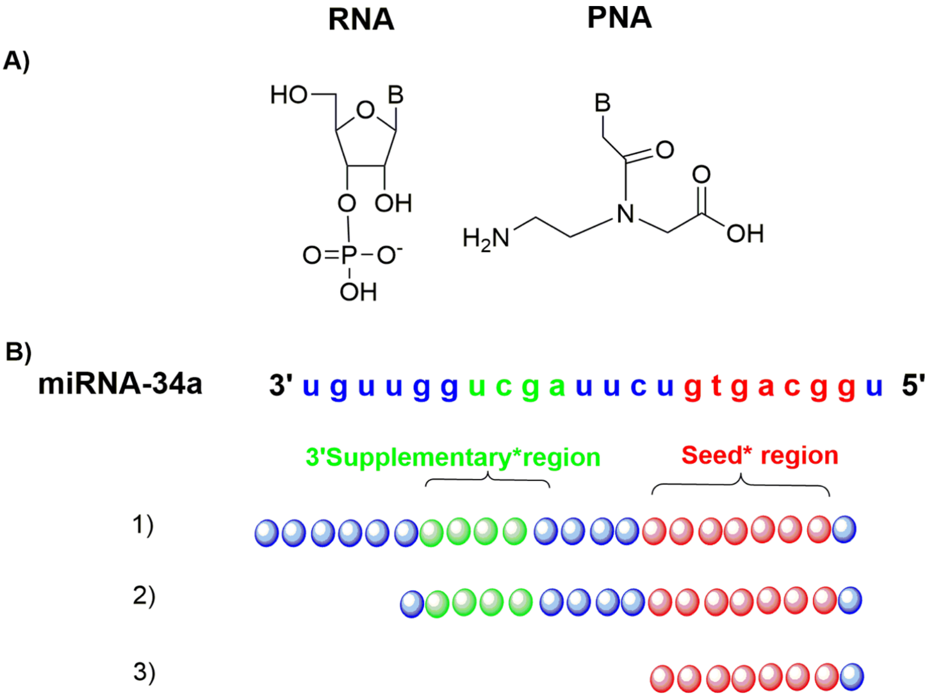

Fig. 2. (A) Chemical structure comparison of RNA and PNA; (B) miRNA-34a sequence and a schematic representation of the design of PNA-based miRNA-34a analogues of different length.

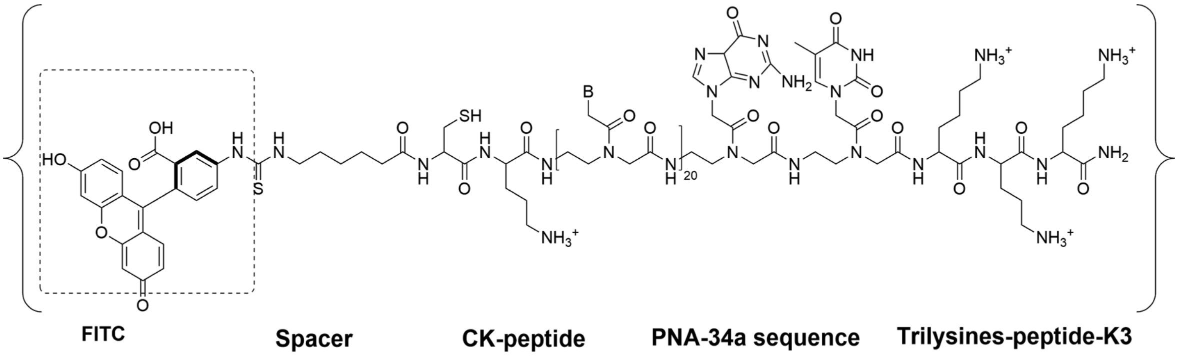

Fig. 3. Chemical structure of PNA-1 FITC sequence.

Fig. 5 (C and D).

However, our data indicate also that the highest RMSD values for seed* regions, are achieved by duplexes containing the longest PNA strand, PNA1. Therefore, the stability of the seed* region slightly decreases by increasing PNA strand length. The stability of seed* regions is revealed also by the analysis of Watson-Crick (WC) hydrogen bonds (Fig. 6). Indeed, for all the studied systems, there is a very high percentage of existence of WC base pairing in the seed* regions, during the whole simulation time, indicating seed regions stability. Few additional hydrogen bonds, having significant percentage of existence, are also present between nucleobases beyond the seed* region in systems RNA1/PNA1, RNA1/PNA2, RNA2/PNA1 and RNA2/PNA2 (Fig. 6). This data suggest that non-seed* regions, including also the 3′ supplementary*, can contribute to the duplex stabilization. For all the simulated systems, three structures were extracted during the simulation at 0 ns, 25 ns and 50 ns, and are shown in Fig. 7. It is noteworthy that, in each system, base pairing as well as double-helix shape in the seed* regions are well-maintained all along the simulation. This finding is in agreement with the high stability of the seed* regions revealed from previous RMSD calculations (Fig. 5) and Watson-Crick hydrogen bonds analyses (Fig. 6).

Beyond the seed* regions, duplexes are significantly distorted due to the presence of many mismatches; however, they never dissociate into the two single strands during simulations. Moreover, in RNA1/PNA3 and RNA2/PNA3 complexes the RNA strand folds on itself forming some additional H-bonds with the PNA strand (in particular in the case of RNA1/PNA3), leading to more compact but disordered structures. This fact can be explained considering the absence of the PNA counterpart for non-seed* RNA residues, therefore the RNA is free to move and probably has affinity to fold back on itself rather than having an elongated conformation.

In summary, the simulation studies show that all the duplexes formed, even if distorted, are stable. Seed* regions are always stable and base-paired; regions beyond the seed*, including 3′ supplementary* regions, also contribute to the duplexes stabilization, as revealed by the formation of some additional hydrogen bonds between nucleobases. However, there is a slightly destabilizing effect on seed* region when the length of the PNA strand increases. All these considerations leads us to hypothesize that PNA2 sequence could truly represent a promising candidate to obtain stable duplexes.

2.3. Physico-chemical characterization: CD and UV melting analysis

The interaction between PNA1-3 sequences and the target 3′UTR MYCN mRNA, as well as the stability of the complexes, were assessed by Circular Dichroism (CD) and UV–VIS spectroscopy. Binding experiments of PNA 1–3 vs. RNA1 and RNA2 were performed by CD; although single stranded PNAs show generally low CD signals [45], PNA/RNA duplexes exhibit characteristic CD signals because of the helicity induced by the chiral RNA in the resulting hybrids (data not shown). Information about secondary structure was also obtained by CD. An overlayed CD profile comparison was elaborated for the three complexes formed, respectively, in binding site 1, RNA1/PNA1, RNA1/PNA2, RNA1/PNA3 (Fig. 8, panel A) and binding site 2 RNA2/PNA1, RNA2/PNA2, RNA2/PNA3 (Fig. 8, panel B). For both binding sites all the complexes showed the typical CD profile of an antiparallel PNA/RNA heteroduplex [46], characterized by two positive maxima at *ca.* 260–270 nm and 220 nm and a negative minimum at *ca.* 240 nm; thus

Table 1
PNA sequences synthesized in this study (N-terminus on the left to C-terminal amide on the right).

Entry	Name	Sequence
1	**PNA1**	Ac-tggcagtgtcttagctggttgt – KKK-NH_2
2	**PNA2**	Ac-tggcagtgtcttagctg – KKK-NH_2
3	**PNA3**	Ac-tggcagtg– KKK-NH_2
4	**PNA1-FITC**	FITC-Ahx -CK -tggcagtgtcttagctggttgt - KKK-NH_2
5	**PNA2-FITC**	FITC- Ahx -CK - tggcagtgtcttagctg – KKK-NH_2
6	**PNA3-FITC**	FITC- Ahx -CK - tggcagtg – KKK-NH_2

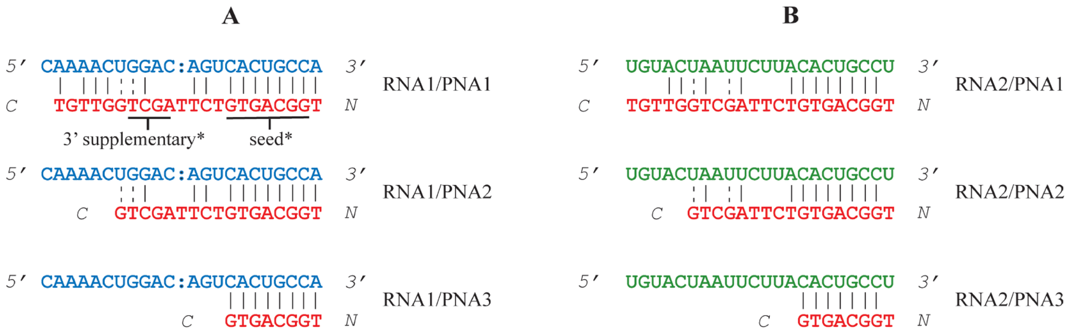

Fig. 4. RNA/PNA complexes studied in this work: Panel A. RNA1 (MYCN mRNA binding site 1), blue; PNAs, red; Panel B. RNA2 (MYCN mRNA binding site 2), green; PNAs, red.

confirming the capability of PNAs to form hetero duplexes with both MYCN 3′UTR mRNA binding sites. The 260–270 nm maximum in both binding sites was shifted to shorter wavelengths, with a larger shift for binding site 2 in terms of both band height and CD value. The maximum at *ca.* 220–210 nm increased in all cases together with the length of the PNA counterpart (from PNA3 to PNA1). The minimum at ca. 240–245 nm had the same sign and similar wavelength for all complexes in both binding sites.

Additionally, UV thermal denaturation experiments of the six complexes RNA/PNA were also carried out evidencing the presence of a sigmoidal-like curves for all the complexes. The overlayed UV-melting curves of the complexes between MYCN mRNA1 (Fig. 8, Panel C) and mRNA2 (Fig. 8, Panel D) with PNA1, PNA2, PNA3 sequences are reported and the corresponding melting temperature (T_m) values are summarized in Table 2.

A similar trend was observed for complexes of PNA1 with both binding sites. The T_m of the full length complexes RNA1/PNA1 and RNA2/PNA1 was 66 °C and 65 °C respectively. The duplex RNA1/PNA2 (17 unit) showed a higher T_m compared to the full-length RNA1/PNA1 $\Delta T_m = 10$ °C; a similar behavior was also observed in binding site 2, with RNA2/PNA1 and RNA2/PNA2 showing a $\Delta T_m = 9$ °C. The destabilization of full-length duplexes RNA1/PNA1 and RNA2/PNA1 compared to the shorter 17-unit PNA2 (RNA1/PNA2 and RNA2/PNA1) can possibly be explained by the presence of mismatched bases at the 5′ of

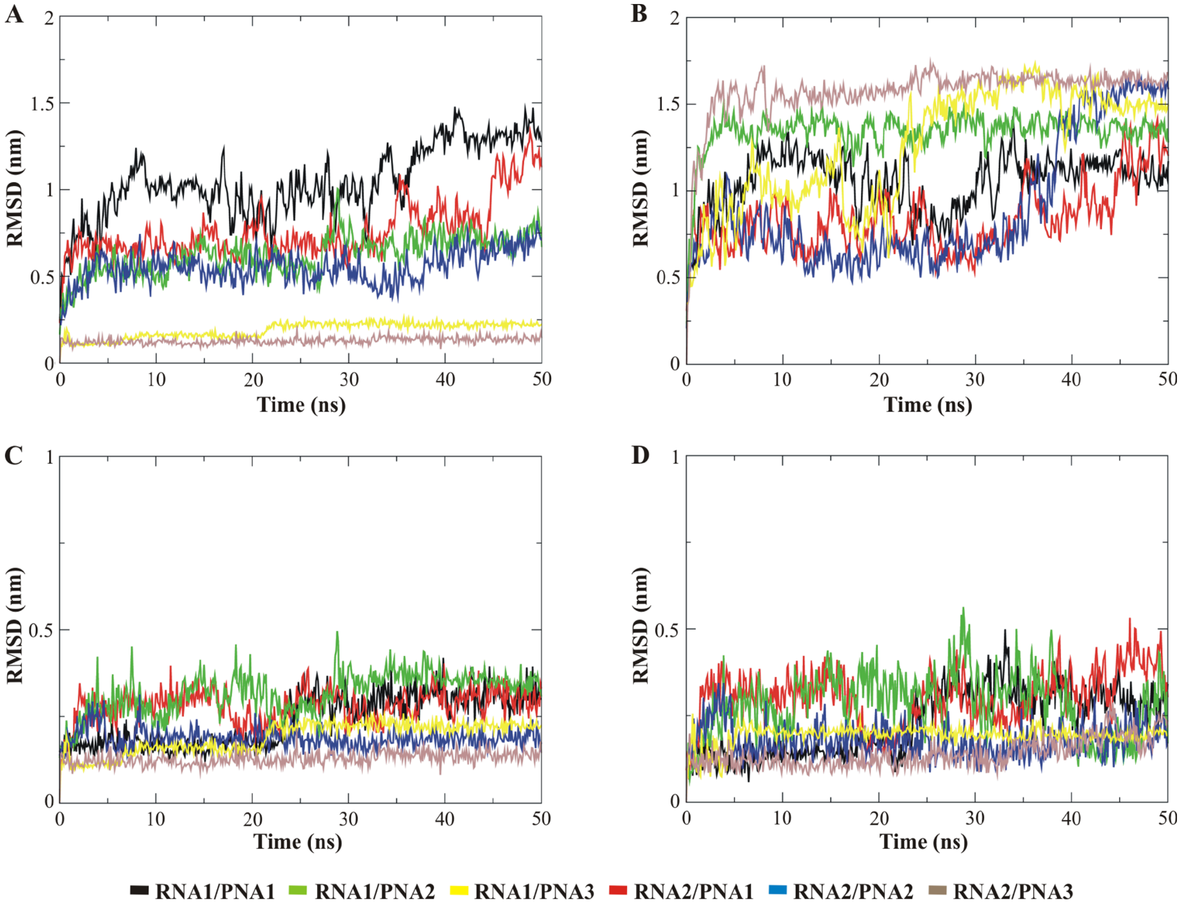

Fig. 5. Root Mean Square Deviation (RMSD) of the six studied duplexes as a function of time. RMSD has been separately computed for: (A) PNA strands, (B) RNA strands, (C) seed* region (2–8 nucleobases) of PNA strands, (D) seed* region of the corresponding RNA strands. Lines are color-coded according to legend.

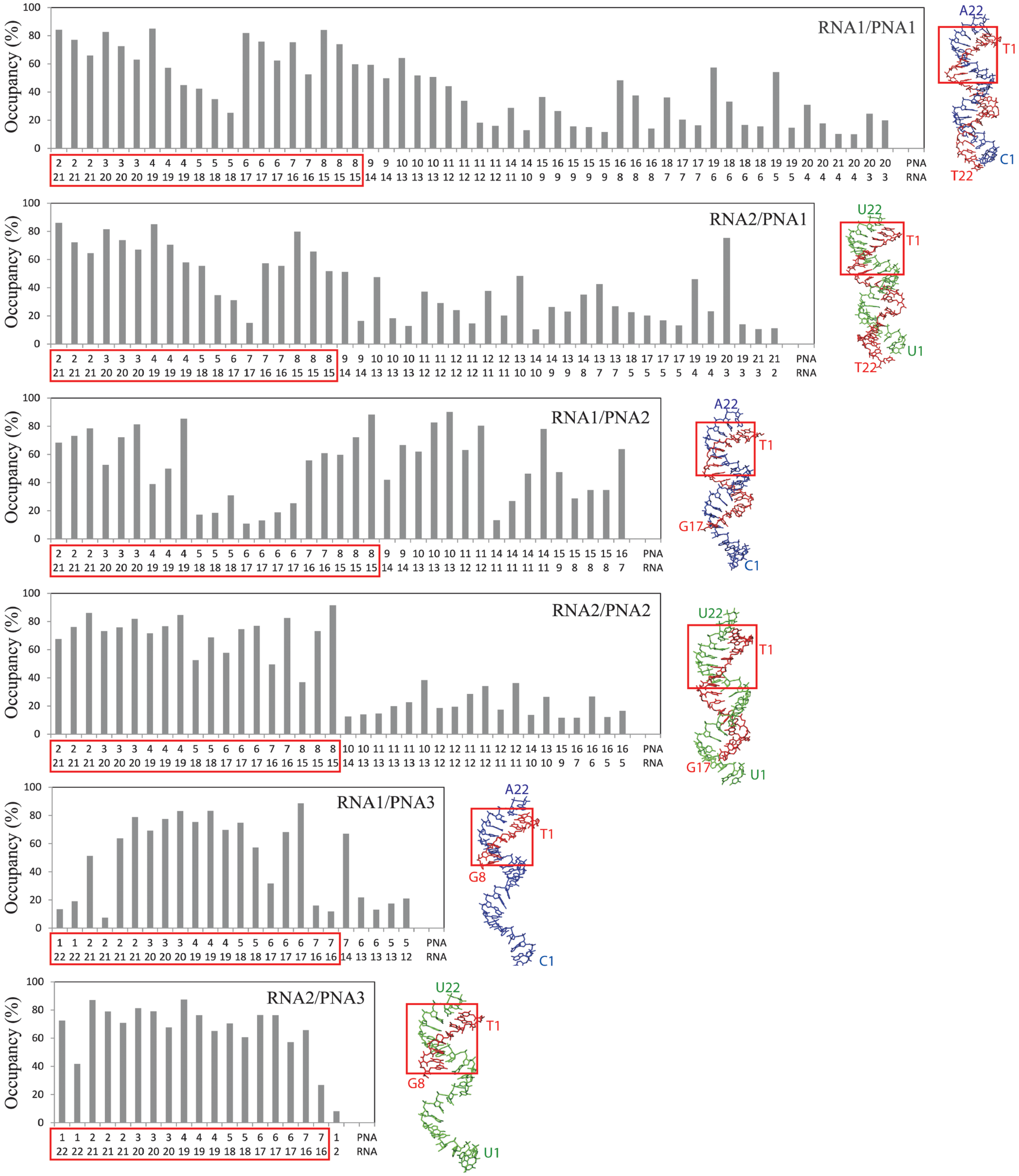

Fig. 6. Percentage of existence (Occupancy) of hydrogen bonds made between nucleobases of the two strands (PNA and RNA) in each system during the simulation time. The couple of nucleobases involved into each hydrogen bond (x axis) has been indicated, using the corresponding nucleobases positions along the sequence. Each RNA/PNA complex has been reported in stick representation using the initial conformation of the corresponding MD simulation. PNA strands are in red, RNA strands are in blue and green for MYCN binding site 1 and MYCN binding site 2, respectively. Seed* regions are boxed in red.

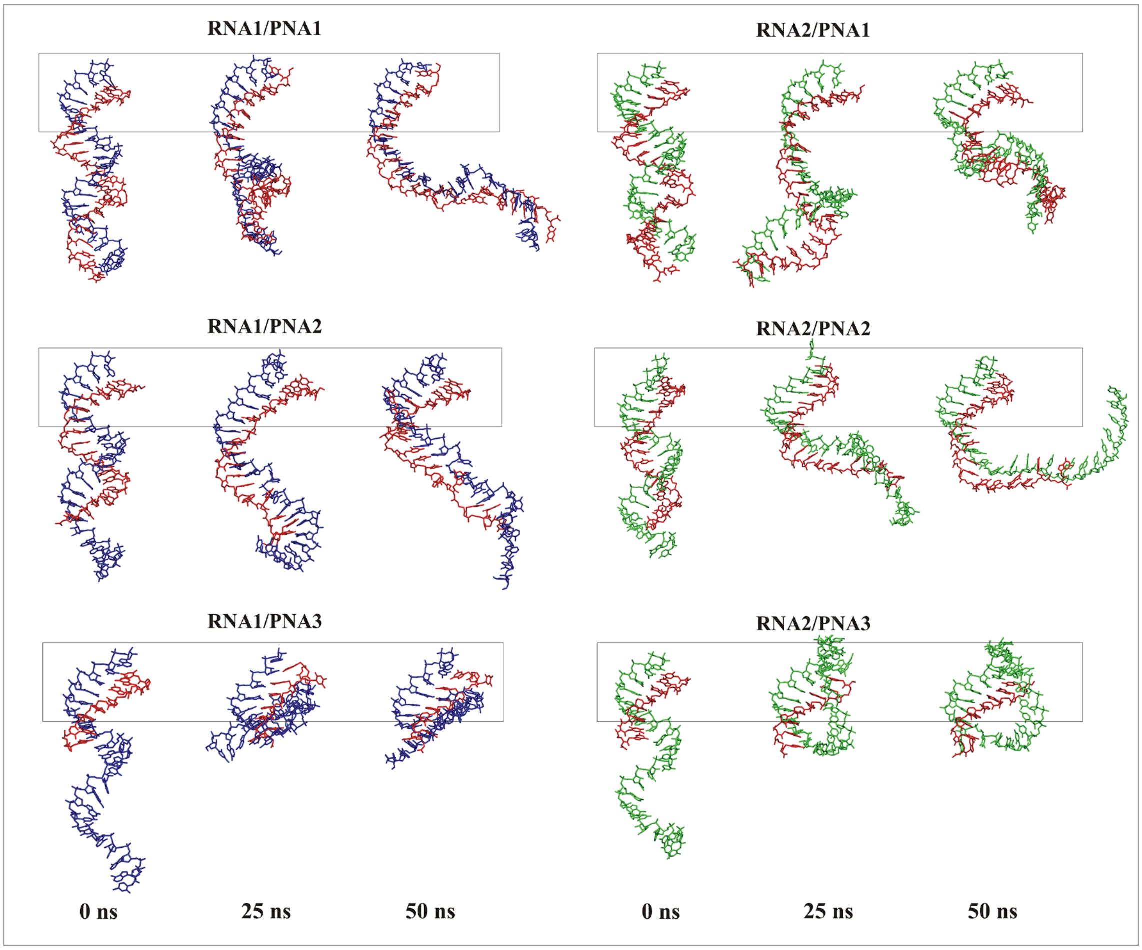

Fig. 7. Representative structures of each simulated system extracted during simulations at 0 ns, 25 ns and 50 ns. PNA strands are in red, RNA strands are in blue and green for MYCN binding site 1 and MYCN binding site 2, respectively. Seed* regions are boxed.

RNA (17–22), causing a drop of stability in the complex [47]. The complex RNA1/PNA3 showed the formation of a complex of higher order with two transitions at $T_{m1} = 35\,^{\circ}C$ $T_{m2} = 77\,^{\circ}C$. It was hypothesized that the longer RNA1 sequence could fold on itself forming some additional H-bonding as also evidenced by MD simulations. The complex RNA2/PNA3 showed a T_m of 75 °C comparable to that of the RNA2/PNA2 (17 unit); this further confirmed the primary stabilization role of the seed* region in target recognition. The melting temperature of the native duplex RNA1/miRNA-34a and RNA2/miRNA-34a are 50 °C and 48 °C respectively (see SI), lower compared to those of RNA1/PNA1 and RNA2/PNA1, thus confirming the advantage of using PNA analogues for RNA targeting even in the presence of multiple mismatches. It should also be noted that, in our study, longer PNA sequences resulted in less stable complexes. This is in agreement with the consequent increase in the number of mismatches and also with MD simulation data. Among all our mimics, PNA2 (17 unit) showed the best balance between length and stability with both binding sites.

2.4. *Preliminary in vitro test in Kelly neuroblastoma cells*

Data collected *in silico* by Molecular Dynamics simulations, then confirmed in solution by spectroscopic studies, encouraged us to bring our investigation to the functional analysis of the PNA sequences *in vitro*. Human Kelly neuroblastoma cell line, was selected to evaluate the cellular uptake of PNA1-3-FITC sequences (entry 4–6 Table 1). The Kelly cell line possesses amplification of the MYCN gene, hence providing high levels of target gene expression. All the sequences for the design relied on the conjugation with cell penetrating peptides consisting of three lysines at the C-terminus, plus a lysine and a cysteine at the N-terminus. This peptide carrier was previously reported by Fabani [41], showing that multiple positive charges provided by the amino groups on the side-chain at physiological pH, along with a free thiol group, was sufficient for the internalization of a 25-mer PNA on Huh7 cells [41]. Kelly cells were incubated for 24 h with PNA1-3 FITC sequences (entries 4–6 Table 1) individually, at minimal 0.1 μM concentration in optiMEM, without the use of any transfecting agent and using a protocol for miRNA mimics delivery, which was previously optimised in the Department of Cancer Genetics [48]. For all sequences PNA 1–3 FITC, the carrier was able to provide internalization (Panel A Fig. 9), albeit to a different extent, which was surprisingly higher for longer sequences. Uptake was not higher than 2% for PNA2-FITC and PNA3-FITC, whereas 15% intake was observed for PNA1-FITC.

The PNA1-3 FITC cellular uptake was also assessed by confocal microscopy (Panel B, Fig. 9). This membrane/nuclei optimal staining protocol and stain compatibility were screened on live and fixed cells in order to achieve the best image resolution. Due to Kelly cells limited adherence to glass-bottomed supports commonly used for the microscope, coverslips were pre-treated with collagen prior to cells being seeded and incubated for 24 h with 2.5 μM solutions for each of PNAs. It was noted that the fluorescence emitted from inside the cell was localized in vesicular shapes in the cytosol. This observation confirmed, as previously reported by Torres et al. [41] with similar constructs, that PNAs conjugated to cationic and thiol-containing CPP were transported inside the cell by different endocytic mechanisms, hence leading to

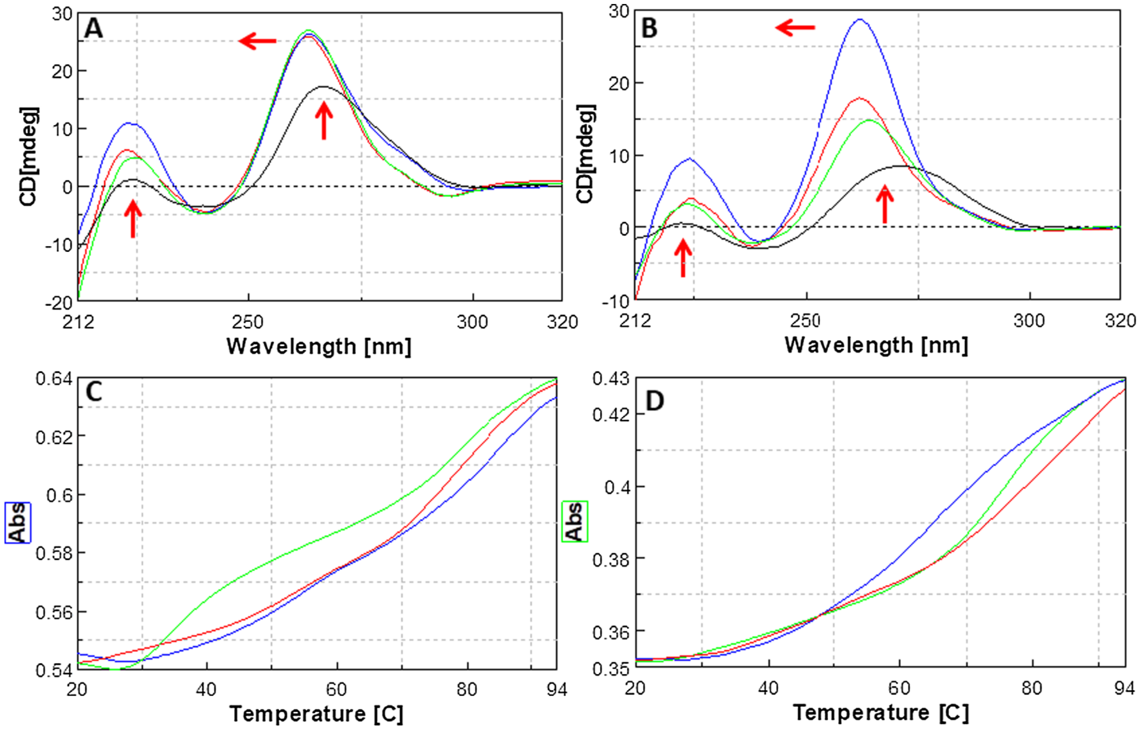

Fig. 8. Conformational analysis of overlayed CD spectra of 2 μm, 100 mM NaCl, 10 mM phosphate buffer pH = 7.4) panel A: RNA1/PNA1 (blue line); RNA1/PNA2 (red line); RNA1/PNA3 (green line); RNA1 (black line); panel B: RNA2/PNA1 (blue line); RNA2/PNA2 (red line); RNA2/PNA3 (green line); RNA2 (black line). Overlayed melting curve of duplexes RNA1-2/PNA 1–3 (2.5 μm, 50 mM NaCl, 5 mM phosphate buffer pH = 7.4) at 260 nm; panel C: RNA1/PNA1 (blue line); RNA1/PNA2 (red line); RNA1/PNA3 (green line); panel D: RNA2/PNA1 (blue line); RNA2/PNA2 (red line); RNA2/PNA3 (green line).

Table 2
Melting temperature for PNA1–3 and RNA1-RNA2 MYCN m-RNA binding sites.

Entry	System	T_m °C (± 0.5)
1	RNA1/PNA1	66
2	RNA1/PNA2	76
3	RNA1/PNA3	T_{m1} = 35 T_{m2} = 77
4	RNA2/PNA1	65
5	RNA2/PNA2	74
6	RNA2/PNA3	75

their incorporation into endosomes. On the other hand, other authors have reported that, in the case of mRNA targeting, endosome trapping could significantly limited the antisense activity [41], which was highly increased by using endosome-disrupting agents such as chloroquine or Ca^{2+} [41]. The cellular uptake of the PNA1-3 FITC was successfully demonstrated in NB cells and represents a promising result considering that intracellular delivery of PNA in some cases still represent a significant challenge. Further *in vitro* studies are currently ongoing to optimize doses and finally assess the functional activity of the PNA sequences as miRNA-34a mimics.

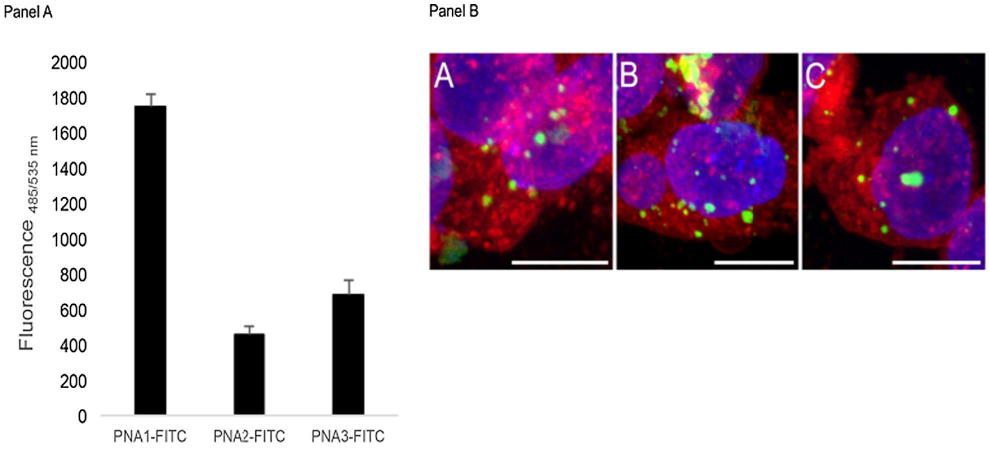

Fig. 9. Panel A: Cellular intake for PNA1-3 FITC at 0.1 μM. All experiments were done on Kelly cells in 3 biological repeats and 4 technical repeats. Panel B: Confocal microscopy of Kelly cells treated with 2.5 μM solution of (a) PNA1-FITC; (b) PNA2-FITC; (c) PNA3-FITC. Green, FITC; red, Cell Mask TM Orange membrane staining; blue, Hoechst DNA staining. Scale bar corresponds to 10 μm in all images. All images were taken at the same confocal microscopy setting.

3. Conclusions

In this work, we have investigated for the first time the use of PNA-based analogues of the tumor suppressive miRNA-34a. PNA 1–3 sequences of different length were designed and synthesized and their interaction with MYCN mRNA binding sites 1 (RNA1) and 2 (RNA2) was investigated *in silico* (MD) and by spectroscopic techniques. In detail, the structural features of PNA1-3/RNA1 and PNA1-3/RNA2 complexes were studied through molecular dynamics simulations using Gromacs. The simulations showed that all PNAs were able to form stable duplexes, albeit distorted to different extents. Seed* regions were base-paired and stable in all cases and 3′ supplementary* regions also contributed to stabilization of the complex, as prompted by the formation of few additional hydrogen bonds. However, a slight destabilizing effect at the seed* region of the PNA:RNA duplex was observed for longer PNA strands. This is in agreement with the consequent increase in number of mismatches. Spectroscopic data confirmed the ability of the PNA1-3 to bind both MYCN mRNA binding sites by forming stable PNA/RNA complexes even in the presence of multiple mismatches. The incomplete complementarity is strictly inherent characteristic of the mechanism of miRNA recognition, and average T_m values for natural RNA-miRNA complex would lie in much lower range compared to the results obtained in this work, thus confirming the advantage of using PNA analogues for RNA targeting. It should also be noted that, in our study, longer PNA sequences resulted in less stable complexes. Among all sequences, both spectroscopic studies and MD confirmed that PNA2 (17 unit) showed the best balance between length and complex stability with both binding sites. Preliminary biological studies comprising uptake assay and confocal microscopy showed that PNA1-3 FITC were able to enter NBL Kelly cells albeit at different extents. This research is a preliminary evaluation of the employment of PNA-based biopolymers as analogues of miRNA-34a; with herein proven high affinity towards nucleic acid targets and ability of forming stable complexes, along with robust fine-tunable synthetic availability and bio conjugation, PNAs represent excellent candidates for miRNA based therapeutics targeting approach.

Nevertheless, further *in vitro* investigation would elucidate how the biological activity of PNA-based analogues could be modulated by fine-tuning the strength of the interaction with its target, obtained by changing the length of the PNA. Also, the combined use of computational and experimental approach would be a powerful tool in the future to guide the design of different sequence pattern of PNA analogues, such as PNA-RNA chimeras. The use of PNA-based or PNA-RNA chimeric miRNA analogues will be explored and tested on different cell lines with or without MYCN amplification and the same approach can be potentially applied to any other opportune miRNAs.

4. Methods

4.1. General information

All starting materials were obtained from commercial suppliers and were used without further purification. Rink amide MBHA resin (100–200 mesh), Fmoc-Lys(Boc)-OH, Fmoc-cys(Trt)-OH, PyBOP (benzotriazol-1-yl-oxytripyrrolidinophosphonium hexafluorophosphate) and N-Methylpyrrolidinone (NMP) were purchased from Novabiochem. Dimethylformamide (DMF), N,N-diisopropylethylamine (DIPEA), Lutidine, piperidine and acetic anhydride were purchased from Sigma-Aldrich. Fmoc-PNA-T-OH, Fmoc-PNA-A(Bhoc)-OH, Fmoc-PNA-C(Bhoc)-OH and Fmoc-PNA-G(Bhoc)-OH were purchased from Link technologies. RNA sequences were purchased by Chem Genes Corporation Wilmington, MA USA.

4.2. Microwave-assisted solid phase PNA synthesis

Solid phase peptide synthesis (SPPS) was carried out on MBHA Rink amide resin 0.59 mmol/g (Novabiochem). Resin was always swollen for 30 min in DMF prior to start any reactions, deprotected from Fmoc group (protocol described below) and downloaded using 0.3 mmol/g of the first residue in chain, followed by acetylation of unreacted amino groups on the solid support (protocol described below). Before storing at −20 °C at the end of every session, the resin was shrunk and dried by multiple washings with DCM, MeOH and diethyl ether in reported order. Coupling of guanine and adenine PNA monomers was always performed twice starting from the 8th monomer on the chain using 3 eq of monomer instead of 4. Also, double coupling was performed for every monomer following a guanine or adenine residue on the chain. The synthesis of PNA1-3 sequence was progressed at 2 μmol scale; whereas the synthesis of PNA1-3 FITC was progressed at 3 μmol scale. Following stock solutions were prepared every 24 h; Fmoc deprotection solution was prepared as 20% piperidine in DMF. Fmoc-amino-acids (0.5 M) and Fmoc-PNA monomers (0.15 M) were dissolved, respectively, in anhydrous DMF or NMP. PyBOP was dissolved at 0.15 M in DMF. PNA capping solution was prepared as a mixture of 5% acetic anhydride and 6% 2,6-lutidine in DMF. Amino acid capping solution was prepared as a mixture of 20% acetic anhydride and 5% DIPEA in DMF. Base solution for aa to aa coupling was prepared as 0.4 M DIPEA solution in NMP. Base solution for PNA to aa or PNA coupling was prepared as 0.15 M DIPEA/0.15 M 2,6-lutidine in NMP. Fmoc deprotection: The resin was treated 3 times with Fmoc deprotection solution for 3 min at r.t. After three cycles the resin was thoroughly washed with DMF and drained. Deprotection solution drained after each cycle was collected. The resulting combined solution was opportunely diluted into a quartz cuvette and the absorbance of dibenzofulvene-piperidine complex was measured by UV spectrometry at 301 nm. The concentration of the complex was calculated by Lambert-Beer law and used to estimate the overall amount of growing polymer anchored on the solid support. Aa to aa coupling: stock solutions of aa (12.5 eq), PyBOP (4 eq), aa coupling base (8 eq) were added onto the solid support and microwaves power was adjusted to the scale to reach 73 °C within 1 min. The temperature was kept constant for 10 min, while the resin was agitated with a gentle stream of nitrogen bubbling through the solution, and then allowed to reach room temperature. The solid support was drained and thoroughly washed with DMF. PNA to aa/PNA coupling*:* stock solutions of PNA residue (4 eq), PyBOP (4 eq), PNA coupling base (8 eq) were added onto the solid support and microwaves were applied to reach 73 °C within 1 min. The temperature was kept constant for 30 min, while the resin was agitated with a gentle stream of nitrogen bubbling through the solution, and then allowed to reach room temperature. The solid support was drained and thoroughly washed with DMF. Capping: Acetylation of unreacted amino groups on the solid support was performed by treating the resin with opportune capping solution (aa or PNA depending on the nature of the amino group to acetylate) for 5 min at r.t. Fluorescein isothiocyanate (FITC) to aminohexanoic acid coupling: 0.2 M FITC (5 eq) in DMF was added onto the solid support in a SPPS vessel and N-methyl morpholine (7 eq) was added. The vessel was kept under agitation in the dark for 2 h then drained and washed with DMF. A second cycle was performed using the same conditions. Cleavage of PNA sequence from the solid support and deprotection: dry resin was treated twice at r.t. for 90 min with 92.5/5/2.5% TFA/m-cresol/TIS (2.5 mL); and EDT (2.5%) was added to cleavage cocktail for PNA1-3 FITC. The resin was filtered off and the solution was treated with cold diethyl ether which was previously stored at −20 °C. The suspension was centrifuged for 30 min at 3000 rpm and the supernatant was discarded. The precipitate was re-suspended with cold diethyl ether and centrifuged. A second resuspension was performed with following centrifugation. The pellet was finally dissolved in 0.1% TFA in water and freeze-dried to afford crude oligomer. PNA sequences were purified by semi-preparative RP-HPLC on a Shimadzu LC-8A, equipped with an SPD-10A VP UV/Vis detector, and on a Hewlett Packard/Agilent 1100 series, equipped with a diode array detector, by using a Phenomenex Jupiter C18 300 Å (10 μm, 10 × 250 mm) column with a flow rate of 5 mL/min. Gradient elution was performed monitoring at 260 nm and 492 nm and a gradient of CH_3CN (0.1% TFA) in H_2O (0.1% TFA) from 5 to 55% in 30 min. PNA oligonucleotide crude and purified product were characterized by Matrix-Assisted Laser Desorption/Ionization (MALDI-TOF MS) using α-cyano-4-hydroxycinnamic acid as a Matrix (10 mg/mL in 50:50 water/acetonitrile (0.1% TFA final concentration); or by LC-MS with a LC-MS Agilent Technologies 6230 ESI-TOF on a Phenomenex Jupiter 3 mm C18 (150 × 20 mm) column with a flow rate of $0.2\,mL\,min^{-1}$. Each pure PNA oligomer was dissolved in a known amount of milliQ water and quantified by UV measurements.

Synthesis of Ac-tggcagtgtcttagctggttgt–KKK-NH_2 (PNA 1): UV quantification of the purified product gave 300 nmol (15%) of PNA 1 LC-ESI MS (*m/z*): 1295.80 (found), 1295.86 (expected for $[M+5H]^{5+}$), 1619.50 (found) 1619.57 expected for $[M+4H]^{4+}$.

Synthesis of Ac-tggcagtgtcttagctg-KKK-NH_2 (PNA 2): UV quantification of the purified product gave 320 nmol (16%) of PNA-2 LC-MS (*m/z*): LC-ESI MS (*m/z*): 1274.04 (found), 1274.25 (expected for $[M+4H]^{4+}$), 1698.38 (found), 1698.66 expected for $[M+3H]^{3+}$.

Synthesis of Ac-tggcagtgt-KKK-NH_2 (PNA 3): UV quantification of the purified product furnished 380 nmol (19%) of PNA 3. LC-ESI MS (*m/z*): 667.79 (found), 667.92 expected for $[M+4H]^{4+}$, 890.06 (found), 890.23 (expected for $[M+3H]^{3+}$), 1334.59 (found), 1334.85 (expected for $[M+2H]^{2+}$).

Synthesis of FITC-Ahx-CK-tggcagtgtcttagctggttgt-KKK-NH_2 (PNA1-FITC): UV quantification of the purified product gave 240 nmol (8%) of PNA1-FITC. MALDI-TOF (*m/z*): $C_{293}H_{373}N_{133}O_{84}S_2$ found 7159.8730 requires 7162.8518, for $[M+H]^+$.

Synthesis of FITC-Ahx-CK-tggcagtgtcttagctg-KKK-NH_2 (PNA2-FITC): UV quantification of the purified product gave 270 nmol (9%) of PNA2-FITC. MALDI-TOF (*m/z*): $C_{238}H_{305}N_{107}O_{66}S_2$, found 5780.5825, requires 5782.3319 for $[M+H]^+$.

Synthesis of FITC-Ahx-CK-tggcagtg-KKK-NH_2 (PNA3-FITC): UV quantification of the purified product gave 330 nmol (11%) of PNA3-FITC. MALDI-TOF (*m/z*): $C_{141}H_{185}N_{60}O_{36}S_2$ found 3358.4622 requires 3358.3926 for $[M+H]^+$.

4.3. Molecular dynamic simulation methods

Dynamic simulation method: MC-Fold-MC-Sym pipeline [49] was used to obtain the three-dimensional model of the duplexes made by miRNA34a with MYCN binding site 1 (RNA1) and binding site 2 (RNA2), respectively. Subsequently, miRNA34a backbone was substituted with the standard *aeg*-PNA backbone, thus obtaining the starting models of RNA1/PNA1 and RNA2/PNA1. Then, RNA1- and RNA2-duplexes with PNA2 and PNA3 where obtained from RNA1/PNA1 and RNA2/PNA1 by removing the PNA exceeding residues. All the systems have been subjected to molecular dynamics (MD) simulations. MD simulations were performed and analyzed using the GROMACS simulation package [43]. The Parmbsc0 [50] force field, a refinement of the AMBER parm9940 force field for nucleic acids [51], was employed for the simulations. Force field parameters derived for PNA from our previous work, were used [44]. The models were solvated in an octahedral box filled with TIP3P water molecules with at least 1.1 Å distance to the border adding counter-ions to neutralize the systems. The simulations were run under NPT conditions (300 K, 1 bar) with the Berendsen coupling algorithm [52]. Periodic boundary conditions were employed and the LINCS algorithm [53] was used to constrain all bond lengths. The particle mesh Ewald method was applied to treat electrostatic interactions [54] and a non bonded cut off of 1.4 nm was used for the Lennard-Jones potential. In all the systems, the water molecules were relaxed by energy minimization and followed by 10 ps of simulations at 300 K, restraining the PNA and RNA atomic positions with a harmonic potential. Then, all the systems were heated up gradually to 300 K in a five step process, starting from 50 K. After this step, the systems were simulated in NPT standard conditions for 50 ns without restraints. The analysis of the MD trajectories was done with the GROMACS package. MOLMOL was used for visual inspection and analysis [55]

4.4. Procedure for the UV absorption measurements and UV-melting experiments

UV measurements were obtained on a JASCO V-550 UV/VIS spectrophotometer equipped with a Peltier block ETC-505T temperature controller by using 1 cm quartz cells of both 0.5 and 1 mL internal volume (Hellma). The concentrations of PNAs were quantified by measuring the absorbance (A260) of the PNA solution at 260 nm. The values for the molar extinction coefficients (ε260) of the individual bases are: ε_{260} (A) = 13.7 mL/(μmole × cm), ε_{260} (C) = 6.6 mL/(μmole × cm), ε_{260} (G) = 11.7 mL/(μmole × cm), ε_{260} (T) = 8.6 mL/(μmole × cm). Molar extinction coefficient of PNA is represented as the sum of those individual bases that comprise the oligomer. $\varepsilon_{260} = \Sigma\, \varepsilon i \times ni$ (εi = molar extinction coefficient of base, ni = number of base). Annealing of all the duplexes was performed by dissolving equimolar amounts of the two complementary strands in milliQ water, heating the solution at 90 °C (5 min) and then allowing to cool slowly to room temperature. Melting curves (at 260 nm) were recorded for a consecutive heating (20–94 °C) -cooling-heating protocol with a linear gradient of 0.5 °C/min. CD Spectra were recorded on a spectrophotometer Jasco −715. CD spectra were recorded at 20 °C using a 1 cm quartz cell using a 320–210 nm measurement range, 50 nm/min scanning speed, 1 nm bandwidth, 4 s response time, 2.0 nm data pitch.

4.5. PNA cellular uptake assay

Kelly cells were seeded in 6-well plates in duplicates at 0.5×10^6 density. After 24 h from incubation, the growth media was replaced with serum-free media (1 mL) and cells were treated with 0.5 mL of 0.3 μM solutions of PNA 1–3 FITC in Opti-MEM. Wells were gently agitated to provide an even treatment of the cells and incubated at 37 °C for 6 h. After incubation, 500 μl of 40% Fetal Bovine Serum (FBS) (Gibco) in RPMI was added to each well. Growth media was removed and wells were incubated at 37 °C for 48 h and washed with 1 mL PBS. Passive Lysis Buffer (Promega) (0.5 mL) was added to each well. The plates were wrapped in tinfoil and placed on the rocker for 20 min. The cell lysates were re-suspended and plated in four replicates on a 96 well plate. The fluorescence of the cell lysate and of the media was read in a dual beam plate reader, at 485/535 nm.

4.6. Confocal microscopy

Eight well coverslips were treated with 0.2 mM solution of collagen in DMEM, and incubated at 0–4 °C overnight. The wells were washed with PBS before seeding. Kelly cells were plated at 10^4 cells/well density. After 48 h from seeding, the growth media was replaced with serum-free media and cells were treated with 200 μl of 2.5 μM solutions of PNA 1–3 FITC in Opti-MEM. Wells were gently agitated to provide an even treatment of the cells and incubated at 37 °C for 6 h. After incubation, 100 μl of 40% FBS in RPMI were added to each well in the 8-well coverslip. After 96 hrs, the cells were gently washed once with PBS, and then treated with 1.5× solution of CellMask™ Plasma Membrane Stains (Thermo Fisher Scientific) in PBS and incubated for 10 min. After this time, the cells were washed twice with PBS, and treated for 10 min with 3.7% EM-grade paraformaldehyde, in PBS, at room temperature. The cells were washed twice with PBS and coverslipped with Vectashield DAPI mounting medium to stain nuclei. The cells were imaged with a Carl Zeiss, LSM 710 confocal Microscope, with images presented as maximum intensity Z projections, to allow for the 2D display of the data. All images were prepared using the FIJI software [56], or the FigureJ Plugin [57].

Acknowledgements

The authors gratefully acknowledge Fondazione con il Sud 2011-DPR-20 for financial support. VP thanks The BioAT (Bioanalysis and Therapeutics) programme of HEA for funding. The authors acknowledge: Prof. R. Stallings and Dr. D. Marasco for suggestions and discussion; Dr. Fintar Kelleher for the access to the microwave facility in IT-Tallaght, M.L. Erby and B. Cavanagh for confocal images.

Appendix A. Supplementary material

Supplementary data to this article can be found online at https://doi.org/10.1016/j.bioorg.2019.103165.

References

[1] (a) M. Ha, V.N. Kim, Nat. Rev. Mol. Cell Biol. 15 (2014) 509–524;
(b) D.P. Bartel, Cell 116 (2) (2004) 281–297.

[2] H.W. Hwang, J.T. Mendell, Br. J. Cancer 94 (6) (2006) 776–780.

[3] (a) D.P. Bartel, Cell 136 (2) (2009) 215–233;
(b) N.D. Brandi, A. Hata, Cell. Commun. Sign 7 (18) (2009) 1–22.

[4] (a) W. Filipowicz, S.N. Bhattacharyya, N. Soneberg, Nat. Rev. Genet. 9 (2008) 102–1149;
(b) V.N. Kim, Nat. Rev. Mol. Cell Biol. 6 (2005) 376–385.

[5] (a) B.D. Adams, A.L. Kasinski, F.J. Slack, Curr. Biol. 24 (16) (2014) R762–R776;
(b) Y. Li, K.V. Kowdley, Genom. Proteom. Bioinformat. 10 (5) (2012) 246–253.

[6] S. Ultimo, G. Zauli, A.M. Martelli, M. Vitale, J.A. McCubrey, S. Capitani, L.M. Neri, Oncotarget 9 (24) (2018) 17238–17254.

[7] (a) Y. Peng, C.M. Croce, Signal Transduct. Target. Ther. 1 (2016) 15004;
(b) D.J. Martin, A.H Lund Anders, Mol. Onc. 6 (6) (2012) 590–610.

[8] S.P. Nana-Sinkam, C.M. Croce, Genome Biol. 15 (2014) 445.

[9] (a) R. Gambari, E. Brognara, D.A. Spandios, E. Fabbri, Int. J. Onc. 49 (2016) 5–32;
(b) M.Y. Shaha, A. Ferrajoli, A.K. Sood, G. Lopez-Berestein, G.A. Calin, EBiomedicine 12 (2016) 34–42.

[10] R. Rupaimoole, F.J. Slack, Nat. Rev. Drug Discov. 16 (3) (2017) 203–222.

[11] E. Anastasiadou, L.S. Jacob, F.J. Slack, Nat. Rev. Cancer 18 (2018) 5–18.

[12] (a) W. Cha, R. Fan, Y. Miao, Y. Zhou, C. Qin, X. Shan, X. Wan, T. Cui Med Chem. Commun. 9 (2018) 396–408;
(b) V. Baumann, J. Winkler, Future Med, Chem. 6 (17) (2015) 1967–1984.

[13] S. Miroshnichenko, O. Patutina, Front. Pharmacol. (2019), https://doi.org/10.3389/fphar.2019.00488.

[14] (a) N. Hosseinahli, M. Aghapour, P.H.G. Duijf, B. Baradaran, J. C. Biol. 233 (8) (2018) 5574–5588;
(b) A.G. Bader, Cancer Res. 70 (18) (2010) 7027–7030.

[15] A.L. Jackson, S.R. Bartz, J. Schelter, S.V. Kobayashi, J. Buchard, M. Mao, B. Li, G. Cavet, P.S. Linsley, Nat. Biotechnol. 21 (2003) 635–637.

[16] (a) A. Ferino, G. Miglietta, R. Picco, S. Vogel, J. Wengel, L.E. Xodo, RNA Biol. (2018) 1–13;
(b) M. Matsui, T.P. Prakash, D.R. Corey, Mol. Ther. 24 (5) (2016) 946–955;
(c) R. Sokilde, I. Newie, H. Persson, A. Borg, C. Rovira, RNA Biol. 12 (8) (2015) 787–791;
(d) G. Chorn, M. Klein-McDowell, L. Zhao, M.A. Saunders, W.M. Flanagan, A.T. Willingham, L.P. Lim, RNA 10 (2012) 1796–1804.

[17] P.E. Nielsen, M. Egholm, M.H. Berg, O. Buchart, Science 254 (1991) 1497–1500.

[18] P.E. Nielsen, M. Egholm, R.H. Berg, O. Buchardt, Antisense Research and Application, CRC Press, Boca Raton, 1993, pp. 363–373.

[19] M. Egholm, O. Buchardt, L. Christensen, C. Behrens, S.M. Freier, D.A. Driver, R. Berg, S.K. Kim, B. Norden, P.E. Nielsen, Nature 365 (1993) 566–568.

[20] M. Egholm, O. Buchardt, P.E. Nielsen, R.H. Berg, J. Am. Chem. Soc. 114 (1992) 9677–9678.

[21] V.V. Demidov, V.N. Potaman, M.D.F. Kamenetskii, M. Egholm, O. Buchart, S.H. Sonnischsen, P.E. Nielsen, Biochem. Pharmacol. 48 (1994) 1310–1313.

[22] M. Moccia, M.F.A. Adamo, M. Saviano, Artificial DNA: PNA & XNA 5 (3) (2016) e1107176, 1–15.

[23] S.H. Lee, E. Moroz, B. Castagner, J.C. Leroux, J. Am. Chem. Soc. 136 (37) (2014) 12868–12871.

[24] A. Gupta, A. Mishra, N. Puri, J. Biotechnol. 59 (2017) 148–159.

[25] (a) J.F. Lima, L. Cerqueira, C. Figueiredo, C. Oliveira, N.F. Azevedo, RNA Biol. 15 (3) (2018) 338–352;
(b) E. Quijano, R. Bahal, A. Ricciardi, W.M. Saltzman, P.M. Glazer, Yale J. Biol. Med. 90 (4) (2017) 583–598;
(c) A.G. Bader, Front. Genet. 3 (2012) 120, 1-9.

[26] F. Zarrilli, F. Amato, C.M. Mordillo, B. Pinto, G. Santarpia, N. Borbone, S. D'Errico, B. Catalanotti, G. Piccialli, G. Castaldo, G. Oliviero, Molecules 22 (2017) 1144.

[27] (a) X.J. Li, Z.J. Ren, J.H. Tang, Cell Death Disease 5 (2014) e1327;
(b) F. Chen, S.J. Hu, J. Biochem. Mol. Toxicol. 26 (2) (2012) 79–86.

[28] (a) M.V. Ruiz-Pérez, A.B. Henley, M.A. Henriksson, Genes 8 (113) (2017) 1–27;
(b) G. Misso, M.T. Di Martino, G. De Rosa, A.A. Farooqi, A. Lombardi, V. Campani, M.R. Zarone, A. Gullà, P. Tagliaferri, P. Tassone, M. Caraglia, Mol. Ther. Nucl. Acid 3 (2014) e-195;
(c) M. Huang, W.A. Weiss, Cold Spring Harbor Perspect. Med. 3 (2013) 10.

[29] J.S. Wei, Y.K. Song, S. Durinck, Q.R. Chen, A.T. Cheuk, P. Tsang, Q. Zhang, C.J. Thiele, A. Slack, J. Shohet, J. Khan, Oncogene 27 (39) (2008) 5204–5213.

[30] G.M. Brodeur, Nat. Rev. Cancer 3 (3) (2003) 203–216.

[31] (a) J.I. Johnsen, C. Dyberg, S. Fransson, Malin Wickström, Pharmacol. Res. 131 (2018) 164–176;
(b) J.M. Maris, M.D. Hogarty, R. Bagatell, S.L. Cohn, The Lancet 369 (9579) (2007) 2106–2120.

[32] L.L. Wang, R. Teshiba, N. Ikegaki, X.X. Tang, A. Naranjo, W.B. London, M.D. Hogarty, J.M. Gastier-Foster, A.T. Look, J.R. Park, J.M. Maris, S.L. Cohn, R.C. Seeger, S. Asgharzadeh, H. Shimada, Br. J. Cancer 113 (1) (2015) 57–63.

[33] (a) V. Zammit, B. Baron, D. Ayers, Genes 9 (1) (2018);
(b) R.L. Stallings, N.H. Foley, P.G. Buckley, I. Bray, Expert Opin. Ther. Targets 14 (2010) 951–962.

[34] (a) M.V. Ruiz-Perez, A.B. Henley, M. Arsenian Henriksson, Genes 8 (2017) 113;
(b) M. Huang, W.A. Weiss, Cold Spring Harbor Perspect. Med. 3 (10) (2013).

[35] (a) F. Megiorni, M. Colaiacovo, S. Cialfi, H.P. McDowell, A. Guffanti, S. Camero, A. Felsani, P.D. Losty, B. Pizer, R. Shukla, C. Cappelli, E. Ferrara, A. Pizzuti, A. Moles, C. Dominici, Oncol. Rep. 38 (2017) 3–20;
(b) J.H. Schulte, S. Horn, T. Otto, B. Samans, L.C. Heukamp, U.C. Eilers, M. Krause, K. Astrahantseff, L. Klein-Hitpass, R. Buettner, A. Schramm, H. Christiansen, M. Eilers, A. Eggert, B. Berwanger, Int. J. Cancer 122 (3) (2008) 699–704.

[36] C. Welch, Y. Chen, R.L. Stallings, Oncogene 26 (34) (2007) 5017–5022.

[37] A. Pession, R. Tonelli, R. Fronza, E. Sciamanna, R. Corradini, S. Sforza, T. Tedeschi, R. Marchelli, L. Montanaro, C. Camerin, M. Franzoni, G. Paolucci, Int. J. Oncol. 24 (2) (2004) 265–272.

[38] R. Tonelli, S. Purgato, C. Camerin, R. Fronza, F. Bologna, S. Alboresi, M. Franzoni, R. Corradini, S. Sforza, A. Faccini, J.M. Shohet, R. Marchelli, A. Pession, Mol. Cancer Ther. 4 (5) (2005) 779–786.

[39] S.A. Gorsky, J. Vogel, J.A. Doudna, Nat. Rev. Mol. Cell Biol. 18 (2017) 215–228.

[40] M. Klein, S.D. Chandradoss, M. Depken, C. Joo, Sem. Cell Dev. Biol. 65 (2017) 20–28.

[41] (a) M.M. Fabani, C. Abreu-Goodger, D. Williams, P.A. Lyons, A.G. Torres, K.G.C. Smith, A.J. Enright, M.J. Gait, E. Vigorito, Nucl. Acid Res. 38 (2010) 4466–4475;
(b) A.G. Torres, M.M. Fabani, E. Vigorito, D. Williams, N. Al-Obaidi, F. Wojciechowski, R.H.E. Hudson, O. Seitz, M.J. Gait, Nucl. Acid Res. 40 (2012) 2152–2167.

[42] B. Bacsa, B. Desai, G. Dibo, C.O. Kappe, J. Peptide Sci. 12 (2006) 633–638.33; M.A. Fara, J.J. Diaz-Mochon, M. Bradley, Tetrahedron Lett. 47 (2006) 1011–1014.

[43] D. Van der Spoel, E. Lindahl, B. Hess, G. Groenhof, A.E. Mark, H.J.C. Berendsen, J. Comput. Chem. 26 (1701e1718) (2005).

[44] (a) I. Autiero, M. Saviano, E. Langella, Phys. Chem. Chem. Phys. 16 (2014) 1868e1874;
(b) I. Autiero, M. Saviano, E. Langella, Eur. J. Med. Chem. 91 (2015) 109–117.

[45] P. Kumar, D.P. Jain, Tetrahedron 71 (2015) 3378–3384.

[46] (a) R. Corradini, T. Tedeschi, S. Sforza, R. Marchelli, Comprehensive Chiroptical Spectroscopy: Applications in Stereochemical Analysis of Synthetic Compounds, John Wiley & Sons Inc, 2012 (cap.18);
(b) M. Egholm, O. Buchart, L. Christensen, C. Behrens, S.M. Freier, D.A. Driver, R.H. Berg, S.K. Kim, B. Norden, P.E. Nielsen, Nature 365 (1993) 566–568.

[47] G.B. Igloi, Proc. Natl. Acad. Sci. USA 95 (1998) 8562–8567.

[48] C. Curtin, J.C. Nolan, R. Conlon, L. Deneweth, C. Gallagher, Y.J. Tan, B.L. Cavanagh, A.Z. Asraf, H. Harvey, S. Miller-Delaney, J. Shohet, I. Bray, F.J. O'Brien, R.L. Stallings, O. Piskareva, Acta Biomater. 70 (2018) 84–97.

[49] M. Parisien, F. Major, Nature 452 (2008) 51–55.

[50] V. Hornak, R. Abel, A. Okur, B. Strockbine, A. Roitberg, C. Simmerling, Proteins 65 (712e725) (2006).

[51] A. Perez, I. Marchán, D. Svozil, J. Sponer, T.E. Cheatham, C.A. Laughton, M. Orozco, Biophys. J. 92 (2007) 3817e3829.

[52] H.J.C. Berendsen, J.P.M. Postma, W.F. Van Gunsteren, A. Di Nola, J.R. Haak, J. Chem. Phys. 81 (1984) 3648e3690.

[53] B. Hess, H. Bekker, H.J.C. Berendsen, J.G.E.M. Fraaije, J. Comput. Chem. 18 (1997) 1463e1472.

[54] (a) T. Darden, D. York, L. Pedersen, J. Chem. Phys. 98 (1993) 10089e10092;
(b) T. Darden, L. Perera, L. Li, L. Pedersen, Structure 7 (1999) R55eR60.

[55] R. Koradi, M. Billeter, K. Wuthrich, J. Mol. Graph. 14 (51–55) (1996) 29–32.

[56] J. Schindelin, I. Arganda-Carreras, E. Frise, V. Kaynig, M. Longair, T. Pietzsch, S. Preibisch, C. Rueden, S. Saalfeld, B. Schmid, J.Y. Tinevez, D.J. White, V. Hartenstein, K. Eliceiri, P. Tomancak, A. Cardona, Nat. Methods 9 (7) (2012) 676–682.

[57] J. Mutterer, E. Zinck, J. Microsc. 252 (1) (2013) 89–91.